LETTER TO THE EDITOR

The *Herschel* Space Observatory view of dust in M81

G. J. Bendo[1], C. D. Wilson[2], M. Pohlen[3], M. Sauvage[4], R. Auld[3], M. Baes[5], M. J. Barlow[6], J. J. Bock[7], A. Boselli[8], M. Bradford[7], V. Buat[8], N. Castro-Rodriguez[9], P. Chanial[4], S. Charlot[10], L. Ciesla[8], D. L. Clements[1], A. Cooray[11], D. Cormier[4], L. Cortese[3], J. I. Davies[3], E. Dwek[12], S. A. Eales[3], D. Elbaz[4], M. Galametz[4], F. Galliano[4], W. K. Gear[3], J. Glenn[13], H. L. Gomez[3], M. Griffin[3], S. Hony[4], K. G. Isaak[14], L. R. Levenson[7], N. Lu[7], S. Madden[4], B. O'Halloran[1], K. Okumura[4], S. Oliver[15], M. J. Page[16], P. Panuzzo[4], A. Papageorgiou[3], T. J. Parkin[2], I. Perez-Fournon[9], N. Rangwala[13], E. E. Rigby[17], H. Roussel[10], A. Rykala[3], N. Sacchi[18], B. Schulz[19], M. R. P. Schirm[2], M. W. L. Smith[3], L. Spinoglio[18], J. A. Stevens[20], S. Sundar[10], M. Symeonidis[16], M. Trichas[1], M. Vaccari[21], L. Vigroux[10], H. Wozniak[22], G. S. Wright[23], W. W. Zeilinger[24]

(Affiliations can be found after the references)

Preprint online version: May 12, 2010

ABSTRACT

We use *Herschel* Space Observatory data to place observational constraints on the peak and Rayleigh-Jeans slope of dust emission observed at 70-500 μm in the nearby spiral galaxy M81. We find that the ratios of wave bands between 160 and 500 μm are primarily dependent on radius but that the ratio of 70 to 160 μm emission shows no clear dependence on surface brightness or radius. These results along with analyses of the spectral energy distributions imply that the 160-500 μm emission traces 15-30 K dust heated by evolved stars in the bulge and disc whereas the 70 μm emission includes dust heated by the active galactic nucleus and young stars in star forming regions.

Key words. Galaxies: ISM – Galaxies: spiral – Galaxies: individual: M81

1. Introduction

The *Herschel* Space Observatory[1] (Pilbratt et al. 2010) provides an unprecedented view of the far-infrared and sub-millimetre emission from nearby galaxies. At wavelengths of 70-160 μm, the PACS instrument (Poglitsch et al. 2010) can produce images with resolutions of 6″-12″ that are superior to what can be achieved with the *Spitzer* Space Telescope. At 250-500 μm, the SPIRE instrument (Griffin et al. 2010) produces images with unprecedented sensitivities to diffuse and point-like submillimetre emission. We can use these data to construct spectral energy distributions (SEDs) that sample the peak and Rayleigh-Jeans side of thermal dust emission, thus allowing us to probe the coldest dust components in nearby galaxies and place superior constraints on dust temperatures and masses. As part of the Very Nearby Galaxies Survey (VNGS), we have imaged the spiral galaxy M81 (NGC 3031) at 70, 160, 250, 350, and 500 μm with PACS and SPIRE. M81 is a nearby (3.63 ± 0.13 Mpc; Freedman et al. 2001) SA(s)ab (de Vaucouleurs et al. 1991) galaxy at an inclination of 59.0° (de Blok et al. 2008) with well defined spiral arms. The *Herschel* data allow us to extract SEDs for ~ 0.7 kpc subregions that are small enough that we can distinguish arm and interarm regions within M81. We use these data to explore the dust temperatures and masses and to understand the heating sources for the dust.

2. Observations and data reduction

The PACS observations were performed as four pairs of orthogonal scans covering $40' \times 40'$ using a 20″ s^{-1} scan rate. PACS can perform simultaneous observations in only two wave bands; we chose the 70 and 160 μm bands since they were expected to bracket the peak of the SED better. The data were reduced using a combination of an adapted *Herschel* Interactive Processing Environment (HIPE) 3.0 pipeline and Scanamorphos (Roussel et al. in prep.). Starting from the raw detector timelines, HIPE was used to mask dead and saturated pixels, convert the signal to Jy pixel^{-1}, and remove cosmic rays. Scanamorphos was then used to map the data while simultaneously removing $1/f$ drifts in the signals. Finally, we subtracted the median backgrounds from the images. The photometric calibration has an accuracy of 10% at 70 μm and 20% at 160 μm, and the full-width half-maxima (FWHM) of the 70 and 160 μm point spread functions (PSFs) are 6″ and 12″, respectively (Poglitsch et al. 2010). The RMS noise levels are 0.12 mJy arcsec^{-2} in both the 70 and 160 μm bands.

The SPIRE observations were performed as two orthogonal scans covering $40' \times 40'$ using a 30″ s^{-1} scan rate. A modified HIPE 3.0 detector timeline pipeline was used to remove cosmic rays, flux calibrate the data, and apply temperature drift and response corrections (see Pohlen et al. 2010, for details). We then removed offsets between the detector timelines in two steps. First, we subtracted the median signal from each bolometer observed during the entire observation. Then we applied an iterative process to remove residual baseline signals that appear as stripes in
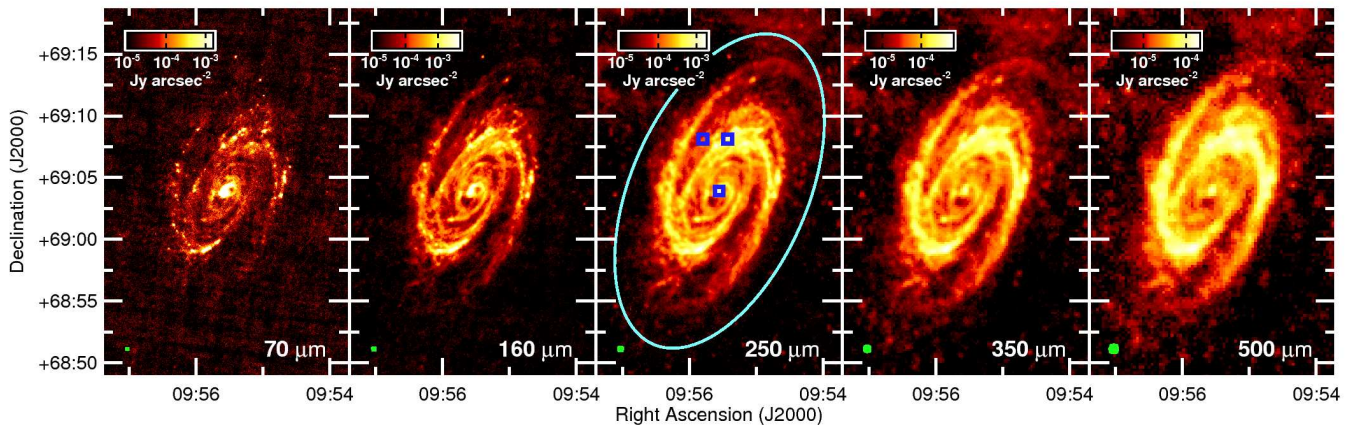
Fig. 1. 70-500 μm images of M81 covering $20' \times 30'$ with north up and east to the left. The images are scaled logarithmically. The green circles in the lower left corner of each image show the FWHM of the PSF. The cyan ellipse in the 250 μm image shows the D_{25} isophote ($26'.9 \times 14'.1$; de Vaucouleurs et al. 1991); the radius is equivalent to 14 kpc. The blue squares in the 250 μm image show the $42''$ regions for which SEDs are plotted in Fig. 4.
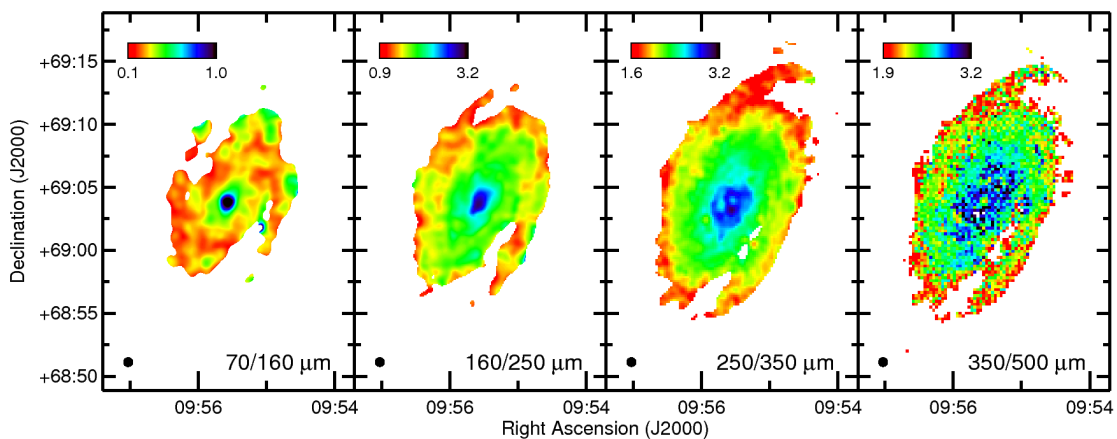
Fig. 2. Images of the 70/160, 160/250, 250/350, and 350/500 μm surface brightness ratios in the optical disc of M81. Each image is created using data with PSFs that match the 500 μm PSF. Regions not detected at the 3σ level in the two bands used for each ratio are left blank. The image sizes and orientations are the same as for Fig. 1. The circles in the lower left corner of each image show the FWHM of the 500 μm PSF.

the maps. In this process, we first created a map. Then, for each bolometer timeline in each scan leg, we measured the signal in the map that corresponded to the bolometer's position, we calculated the median difference between the bolometer signal and the corresponding map signal, and we subtracted this function from the bolometer signal. These steps were repeated 40 times to completely remove stripes from the data. Finally, we subtracted median background signals from the images. The resulting images have flux calibration uncertainties of 15%, and the 250, 350, and 500 μm PSFs have FWHM of $18''$, $25''$, and $37''$, respectively (Swinyard et al. 2010). The RMS noise levels are 0.040, 0.019, and 0.008 mJy arcsec^{-2} in the 250, 350, and 500 μm bands, respectively.

To create ratios of surface brightnesses measured in two wave bands, we matched the PSFs, which we treated as Gaussian, to the PSF of the 500 μm data. For statistical analyses on surface brightness ratios and for creating SEDs of subregions within the galaxies, we then rebinned the data in all images into $42''$ (~ 0.7 kpc) square pixels (selected because it is an integer multiple of the 500 μm pixel size

that is larger than the PSF FWHM for the 500 μm data). For these analyses, we only used used $42''$ pixels with 3σ detections in all bands.

3. Results

Figure 1 shows the structures traced by the various *Herschel* wave bands, which look very similar to each other and to the 5.7-24 μm *Spitzer* images (Gordon et al. 2004; Willner et al. 2004). All images trace the same spiral structure and individual infrared sources within the disc of the galaxy. Diffuse, extended sources detected outside the optical disc of M81 in the *Herschel* data seem most likely to be associated with dust in the Milky Way (Davies et al. in prep.).

To understand the heating mechanism for the dust, we examined how surface brightness ratios varied with surface brightness and with radius. Variations with surface brightness would suggest that the dust is heated locally and that the emission is linked to star formation, whereas radial variations in the ratios would indicate that the dust emission
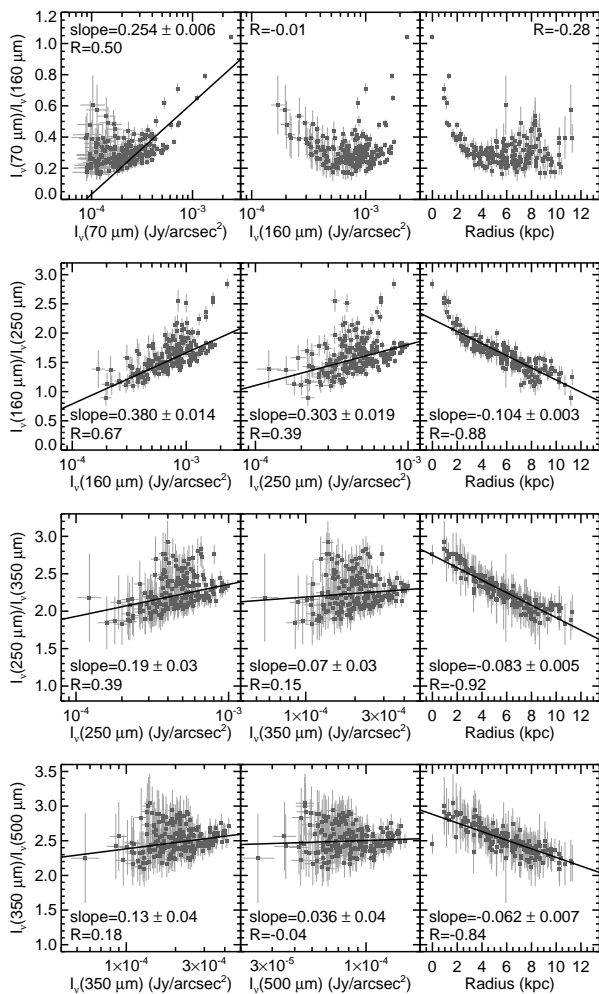
Fig. 3. The 70/160, 160/250, 250/350, and 350/500 μm surface brightness ratios versus the surface brightness (left and center) and inclination-corrected galactocentric radius (right). The data were measured in 42″ subregions in images with PSFs that matched the PSF of the 500 μm data. Best fit lines are shown for all plotted data except for two relations involving the 70/160 μm ratio, where the fits were very poor; corresponding slopes are given in the panels. The R values are the Pearson correlation coefficients for the plotted data. Note that, in the left-side and center panels, the logarithm of the surface brightnesses are used for the best fit lines and correlation coefficients.

is more strongly affected by the evolved stellar populations in the bulge and disc. Figure 2 shows images of the 70/160, 160/250, 250/350, and 350/500 μm surface brightness ratios. Additionally, Fig. 3 shows how the ratios measured in 42″ (~ 0.7 kpc) subregions vary with surface brightness and galactocentric radius.

The absolute value of the correlation coefficient R for the relations between radius and either the 160/250, 250/350, or 350/500 μm ratios is generally higher than that for the relations between surface brightness and the ratios, which shows that these ratios are more strongly dependent on radius (although the 160/250 μm ratio may also be partly dependent on 160 μm surface brightness based on the high value of R). This is consistent with the weak or absent infrared-bright regions or spiral structure in the
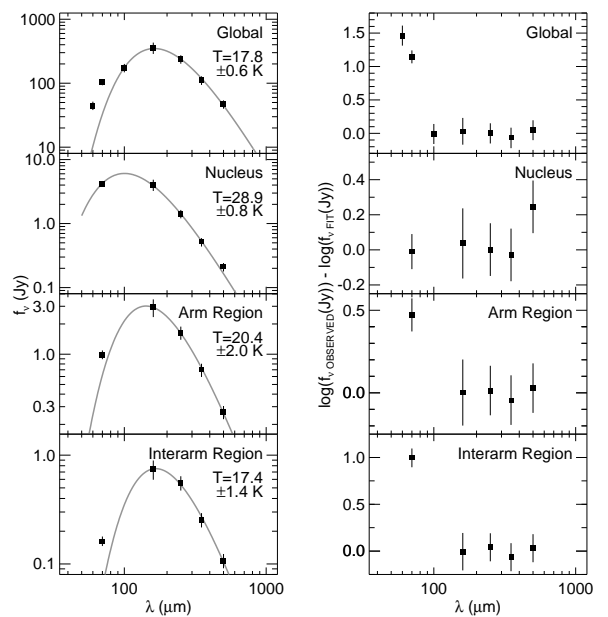
Fig. 4. On the left, the global SED as well as the SEDs for the three 42″ (~ 0.7 kpc) regions shown in Fig. 1. The SEDs for the subregions were measured in data with PSFs that matched to the PSF of the 500 μm data. The grey line is the blackbody modified with a λ^{-2} emissivity function fit to the data. On the right are the residuals from the fit in logarithm space.

images of the 160/250, 250/350, and 350/500 μm ratios. Moreover, the R^2 values, which equal the fraction of the variance in the data that can be accounted for by the best fit line, indicate that $>70\%$ of the variance in the 160/250, 250/350, and 350/500 μm ratios can be accounted for by the relation with radius.

In contrast, the 70/160 μm ratio does not vary monotonically with radius except within 2 kpc, a region in which the gradient in the 160/250 μm ratio also increases. This could represent enhanced dust heating within this radius that is powered by the active galactic nucleus (AGN), by strong central star formation activity, or by the bulge stars, which have a high central density. The 70/160 μm ratio versus 160 μm surface brightness exhibits no obvious trend and only a statistically weak trend (with $R^2 < 0.3$) is visible in the plot of the 70/160 μm ratio versus 70 μm surface brightness, although the best fit line poorly describes the data. None the less, Fig. 2 shows that the ratio increases to $\gtrsim 0.3$ in infrared-bright regions in the spiral arms.

Figure 4 shows the SED integrated across the optical disc (with supplemental 60 and 100 μm IRAS data added from Rice et al. (1988)) as well as the SEDs for the 42″ regions centered on the nucleus, and examples of an infrared-bright source and an interarm region. Based on visually inspecting and fitting functions to the SEDs, these example regions were typical to similar regions at similar radii. In the nucleus, we were able to fit a single blackbody modified with a λ^{-2} emissivity function (based on the Li & Draine (2001) emissivity function) to the 70-350 μm data, but the 500 μm data point could not be fit with the same thermal component, although the mismatch between the fit and model is only 2σ. This result and the low 350/500 μm ratio for the nucleus seen in Fig. 3 (which is 3σ below the best fit line)

suggest that the 500 μm nuclear emission likely includes a non-thermal component associated with the AGN. Based on the SED fit, we estimate that the non-thermal 500 μm emission is 0.05 ± 0.03 Jy, which is $\sim 2.5\times$ below a power law extrapolated from the mm and cm data presented by Markoff et al. (2008). The discrepancy could be explained by the low signal-to-noise in the estimate from the SED fit or by variability in the AGN emission; the 870 μm flux density has been observed to vary by $3\times$ (Markoff et al. 2008).

In the other SEDs, we found that single blackbodies modified with λ^{-2} emissivity functions could be fit accurately to the >100 μm data without the fit overpredicting the observed 70 μm measurement, but fits that included the 70 μm data point did not accurately replicate the peak of the SED. No evidence is found for the excess emission at submillimetre wavelengths sometimes attributed to dust with < 10 K temperatures or shallow emissivities, although prior results had indicated that this emission would be more prominent at >500 μm (e.g. Galliano et al. 2005; Bendo et al. 2006; Zhu et al. 2009; O'Halloran et al. 2010). By applying to the data for the global SED the equation $M_{dust} = [f_\nu D^2]/[\kappa B(\nu, T)]$ (where D is distance, κ_ν is the dust opacity from Li & Draine (2001), and $B(\nu, T)$ is the best fitting modified blackbody), we estimated the global dust mass to be $3.4 \pm 0.5 \times 10^7$ M$_\odot$. Given that the atomic gas mass is $3.64 \pm 0.18 \times 10^9$ M$_\odot$ (Walter et al. 2008) and the molecular gas mass is negligible in comparison (Sage 1993, Sánchez-Gallego et al. in prep.), we estimate that the gas-to-dust ratio is 107 ± 17, which is within the range of ~ 100-200 expected for solar metallicity objects based on the depletion of metals from the gaseous phase of the interstellar medium or comparisons of gas column density to dust extinction (e.g Whittet 2003). Hence, this simplistic modified blackbody fit may be a fair representation of the emission from the bulk of the dust mass in M81, although more sophisticated modeling should not only yield more accurate masses but also describe the emission from warmer dust components.

The SED fits along with the results from Figs. 2 and 3 imply that the 70 μm band traces dust heated by a different source than the dust that primarily emits in the 160-500 μm bands. Although the 70/160 μm ratio exhibits a lot of scatter, the enhancements in the 70/160 μm ratio in the spiral arms implies that the 70 μm band may be affected by star formation on local scales. Meanwhile, the radial variations in the 160-500 μm ratios and the SED fits suggest that $\sim 20\%$ of the 60 μm emission, $\sim 30\%$ of the 70 μm emission, and $\sim 100\%$ of the > 100 μm emission originates from dust heated by evolved disc and bulge stars. This is consistent with prior results suggesting that ~ 5-100% of the 60 and 100 μm emission from nearby galaxies originates from dust heated by evolved stars (e.g. Sauvage & Thuan 1992; Walterbos & Greenawalt 1996). If this interpretation is correct, we anticipate that dust emitting at 160-500 μm in other galaxies with relatively large fractions of old stars (E-Sab galaxies) will also have 160-500 μm colours that depend upon radius, but galaxies with relatively large fractions of young stars (Sc-Im galaxies) will have 160-500 μm colours that may depend more on infrared surface brightness, as heating by the evolved stellar population becomes insignificant. The results also imply that the conversion of infrared fluxes integrated over very broad ranges (e.g. 8-1000 μm) to star formation rates, as done by Zhu et al.

(2008), Rieke et al. (2009), and Kennicutt et al. (2009), will be accurate as long as the integrals contain a significant amount of emission shortward of 160 μm that traces dust heated by star formation. However, it may not be possible to derive accurate star formation rates from dust emission measured solely at >160 μm.

In conclusion, these results for M81 demonstrate how *Herschel* 70-500 μm data can be used to not only measure more accurate dust temperatures and masses but also determine the dust heating sources in nearby galaxies. Further work with data from the VNGS and other surveys will allow us to determine whether dust traced by the 160-500 μm bands in other spiral galaxies is also heated by evolved stellar populations and whether variations in the relative strength of dust heating by evolved stars varies across the Hubble sequence.

References

Bendo, G. J., Dale, D. A., Draine, B. T., et al. 2006, ApJ, 652, 283
de Blok, W. J. G., Walter, F., Brinks, E., et al. 2008, AJ, 136, 2648
de Vaucouleurs, G., de Vaucouleurs, A., Corwin, H. G., et al. 1991, Third Reference Catalogue of Bright Galaxies (Springer-Verlag, Berlin)
Freedman, W. L., Madore, B. F., Gibson, B. K., et al. 2001, ApJ, 553, 47
Galliano, F., Madden, S. C., Jones, A. P., Wilson, C. D., & Bernard, J.-P. 2005, A&A, 434, 867
Gordon, K. D., Pérez-González, P. G., Misselt, K. A., et al. 2004, ApJS, 154, 215
Griffin, M., et al. 2010, A&A, this volume
Kennicutt, R. C., Jr., Hao, C.-N., Calzetti, D., et al. 2009, ApJ, 703, 1672
Li, A., & Draine, B. T. 2001, ApJ, 554, 778
Markoff, S., Nowak, M., Young, A., et al. 2008, ApJ, 681, 905
O'Halloran, B., Galametz, M., Madden, S., et al. 2010, A&A, this volume
Pilbratt, G., et al. 2010, A&A, this volume
Poglitsch, A., et al. 2010, A&A, this volume
Pohlen, M., Cortese, L., Smith, M. W. L., et al. 2010, A&A, this volume
Rice, W., Lonsdale, C. J., Soifer, B. T., et al. 1988, ApJS, 68, 91
Rieke, G. H., Alonso-Herrero, A., Weiner, B. J., et al. 2009, ApJ, 692, 556
Sage, L. J. 1993, A&A, 272, 123
Sauvage, M. & Thuan, T. X. 1992, ApJ, 396, L69
Swinyard, B. M., Ade, P. A. R., Baluteau, J.-P., et al. 2010, A&A, this volume
Walter, F., Brinks, E., de Blok, W. J. G., et al. 2008, AJ, 136, 2563
Walterbos, R. A. M., & Greenawalt, B. 1996, ApJ, 460, 696
Willner, S. P., Ashby, M. L. N., Barmby, P., et al. 2004, ApJS, 154, 222
Whittet D. C. B. 2003, Dust in the Galactic Environment, Second Edition (Institute of Physics Publishing, Bristol, United Kingdom)
Zhu, M., Papadopoulos, P. P., Xilouris, E. M., Kuno, N., & Lisenfeld, U., 2009, ApJ, 706, 941

Zhu, Y. N., Wu, H., Cao, C., & Li, H.-N. 2008, ApJ, 686, 155

[1] Astrophysics Group, Imperial College, Blackett Laboratory, Prince Consort Road, London SW7 2AZ, UK e-mail: `g.bendo@imperial.ac.uk`

[2] Dept. of Physics & Astronomy, McMaster University, Hamilton, Ontario, L8S 4M1, Canada

[3] School of Physics and Astronomy, Cardiff University, Queens Buildings The Parade, Cardiff CF24 3AA, UK

[4] Laboratoire AIM, CEA/DSM - CNRS - Université Paris Diderot, Irfu/Service d'Astrophysique, 91191 Gif sur Yvette, France

[5] Sterrenkundig Observatorium, Universiteit Gent, Krijgslaan 281 S9, B-9000 Gent, Belgium

[6] Department of Physics and Astronomy, University College London, Gower Street, London WC1E 6BT, UK

[7] Jet Propulsion Laboratory, Pasadena, CA 91109, United States; Department of Astronomy, California Institute of Technology, Pasadena, CA 91125, USA

[8] Laboratoire d'Astrophysique de Marseille, UMR6110 CNRS, 38 rue F. Joliot-Curie, F-13388 Marseille France

[9] Instituto de Astrofsica de Canarias, C/Vía Láctea s/n, E-38200 La Laguna, Spain

[10] Institut d'Astrophysique de Paris, UMR7095 CNRS, Université Pierre & Marie Curie, 98 bis Boulevard Arago, F-75014 Paris, France

[11] Department of Physics & Astronomy, University of California, Irvine, CA 92697, USA

[12] Observational Cosmology Lab, Code 665, NASA Goddard Space Flight Center Greenbelt, MD 20771, USA

[13] Department of Astrophysical & Planetary Sciences, CASA CB-389, University of Colorado, Boulder, CO 80309, USA

[14] ESA Astrophysics Missions Division, ESTEC, PO Box 299, 2200 AG Noordwijk, The Netherlands

[15] Astronomy Centre, Department of Physics and Astronomy, University of Sussex, UK

[16] Mullard Space Science Laboratory, University College London, Holmbury St Mary, Dorking, Surrey RH5 6NT, UK

[17] School of Physics & Astronomy, University of Nottingham, University Park, Nottingham NG7 2RD, UK

[18] Istituto di Fisica dello Spazio Interplanetario, INAF, Via del Fosso del Cavaliere 100, I-00133 Roma, Italy

[19] Infrared Processing and Analysis Center, California Institute of Technology, Mail Code 100-22, 770 South Wilson Av, Pasadena, CA 91125, USA

[20] Centre for Astrophysics Research, Science and Technology Research Centre, University of Hertfordshire, College Lane, Herts AL10 9AB, UK

[21] University of Padova, Department of Astronomy, Vicolo Osservatorio 3, I-35122 Padova, Italy

[22] Observatoire Astronomique de Strasbourg, UMR 7550 Université de Strasbourg - CNRS, 11, rue de l'Université, F-67000 Strasbourg

[23] UK Astronomy Technology Center, Royal Observatory Edinburgh, Edinburgh, EH9 3HJ, UK

[24] Institut für Astronomie, Universität Wien, Türkenschanzstr. 17, A-1180 Wien, Austria